
Parametrizing Convex Sets Using Sublinear Neural Networks

Eloi Martinet

Institute for Mathematics,
University of Würzburg
Germany

eloi.martinet@uni-wuerzburg.de

Abstract

We propose a neural parameterization of convex sets by learning sublinear (positively homogeneous and convex) functions. Our networks implicitly represent both the support and gauge functions of a convex body. We prove a universal approximation theorem for convex sets under this parametrization. Empirically, we demonstrate the method on shape optimization and inverse design tasks, achieving accurate reconstruction of target shapes.

1 Introduction

1.1 Convex Shape Optimization

Shape optimization under convexity constraints has been extensively studied due to its analytical tractability and practical relevance [1]. Early numerical approaches enforced convexity through penalization, notably via the distance to the convex hull [2]. Alternative formulations characterized convex sets as intersections of half-spaces [3], which guarantee convexity but limit the representation of smooth geometries.

A widely adopted paradigm relies on functional parametrization using support or gauge functions [4]. These approaches enable compact representations and have been successfully applied in various contexts [5–9]. However, convexity is encoded through second-order differential inequalities, leading to constrained optimization problems that are difficult to handle, especially in higher dimensions. While exact enforcement is possible in two dimensions [6, 7], extensions to three dimensions always rely on relaxations that may compromise convexity [5] [10].

Geometric approaches provide an alternative by directly constraining admissible deformations. For instance, [11] proposes a triangulation-based framework ensuring convexity preservation through restrictions on the deformation field, while [12] makes use of Minkowski deformations.

1.2 Neural Representations of Convex Sets

In the last years, a significant amount of work has been devoted to interfacing or replacing classical topology optimization methods with neural networks, parametrizing the shape using a neural network or making use of Physics Informed Neural Networks (PINNs) to solve the underlying state equation (see e.g. [13] for a review). Recent advances in machine learning have introduced flexible neural representations of shapes with built-in properties. For instance, [14] enforces a volume constraint using SympNets; convexity can be enforced at the level of level-set functions [15] using for instance input-convex neural networks (ICNNs) [16].

Beyond shape optimization, convex shape priors have been used as an inductive bias in image segmentation [17] or for convex decomposition through diffuse interface formulations such as

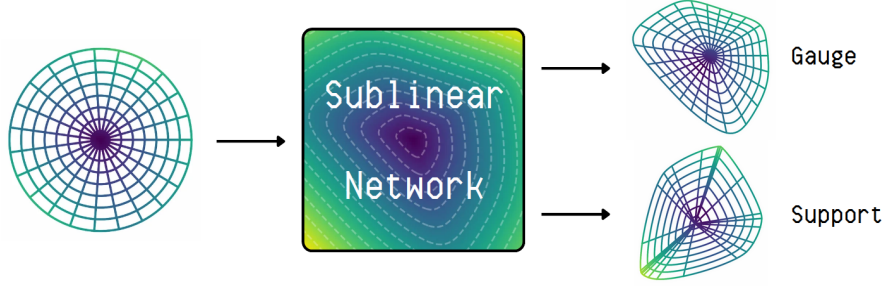


Figure 1: A sublinear network can represent both the gauge and support functions of convex sets, and allow to parameterize smooth bijections that sends the ball on convex sets.

phase-field models [18]. In [19], it is shown that convexity is an important property of the latent representation of decision regions.

1.3 Main contributions

Despite these advances, classical approaches faces significant challenges, like exact enforcement of constraints (especially in three dimensions) or flexibility when it comes to the computation of shape-related quantities. On the other hand, neural approaches often rely on implicit parametrization that makes the computation of boundary quantities harder.

In contrast, our approach aims to combine the strengths of these paradigms by providing a representation that: (i) ensures exact convexity without constraints, (ii) can represent any convex set, (iii) allows for simple and precise computation of higher-order geometric terms and (iv) is able to seamlessly treat different dimensions. We demonstrate these claims on various inverse and shape optimization problems, like shape reconstruction or the maximization of the torsional rigidity of a rod.

From a machine learning perspective, our approach can be interpreted as defining a hypothesis class of neural networks that encode convexity exactly by construction. In contrast to ICNNs, which enforce convexity of scalar functions with respect to inputs, our architecture directly parameterizes convex bodies. This provides an inductive bias tailored to geometric learning problems, enabling both expressive representations and efficient computation of shape-dependent quantities.

2 Parametrization of convex sets using neural networks

2.1 Gauge and support functions

In what follows, \mathcal{K} represents the set of convex bodies in \mathbb{R}^d (i.e. compact convex sets with non-empty interior [20]) which contains 0 in their interior. Commonly associated with a convex set $\Omega \in \mathcal{K}$ are the gauge and support functions, respectively defined as

$$g_{\Omega}(u) := \inf \{ \lambda \geq 0 : u \in \lambda\Omega \} \quad \text{and} \quad h_{\Omega}(u) := \sup_{x \in \Omega} x \cdot u$$

for $u \in \mathbb{R}^d$. It can readily be seen that both of these functions are *sublinear*, i.e. subadditive and positively homogeneous. Reciprocally, if $f : \mathbb{R}^d \rightarrow \mathbb{R}$ is a sublinear function, then it is respectively the gauge and support function of the convex sets (see [20, Theorem 1.7.1])

$$\{x \in \mathbb{R}^d : f(x) \leq 1\} \quad \text{and} \quad \{x \in \mathbb{R}^d : x \cdot y \leq f(y) \text{ for all } y \in \mathbb{R}^d\} \quad (1)$$

We can use the gauge function of a convex Ω to give an explicit parametrization of Ω as the image of the unit ball $B \subset \mathbb{R}^d$ in the following way:

Proposition 2.1. *Let g be a positive and sublinear function. The function $\phi : x \mapsto \frac{\|x\|}{g(x)}x$ (extended by 0 at the origin) is a homeomorphism from B to $\phi(B)$ and the image set $\phi(B)$ is convex with gauge function g .*

Proof. Let $\Omega := \{y \in \mathbb{R}^d : g(y) \leq 1\}$. For $x \in B$, we have $g(\phi(x)) = \frac{\|x\|}{g(x)}g(x) = \|x\| \leq 1$. Hence, $\phi(B) \subset \Omega$. On the other hand, if $y \in K$, then $x := \phi^{-1}(y) = \frac{g(y)}{\|y\|}y \in B$ and $y = \phi(x)$. Therefore, $\phi(B) = \Omega$ is convex and ϕ is a homeomorphism. \square

Using [20, Corollary 1.7.3], we know that if $\Omega \in \mathcal{K}$ is such that h_Ω is differentiable on $\mathbb{R}^d \setminus \{0\}$, then $\nabla h_\Omega : \mathbb{S}^{n-1} \rightarrow \partial\Omega$ is a homeomorphism. This leads to the following proposition:

Proposition 2.2. *Let h be a positive and sublinear function, differentiable on $\mathbb{R}^d \setminus \{0\}$. The function $\phi : x \mapsto \|x\|\nabla h(x)$ (extended by 0 at the origin) is bijective from B to $\phi(B)$ and the image set $\phi(B)$ is convex with support function h .*

Proof. According to the assumptions, there exists $\Omega \in \mathcal{K}$ such that $h = h_\Omega$. Let $y \in \tilde{\Omega} := \phi(B)$. Then there exists $x \in B$ such that $y = \|x\|\nabla h_\Omega(x) \in \text{Conv}(\partial\Omega \cup \{0\})$; indeed, since $0 = \phi(0) \in \tilde{\Omega}$ and $\|x\| \leq 1$, y is a convex combination of 0 and $\nabla h_\Omega(x) \in \partial\Omega$ (here, we used that ∇h_Ω is 0-homogeneous). Since K is a compact convex set, $\text{Conv}(\partial K \cup \{0\}) = \Omega$ and hence $\tilde{\Omega} \subset \Omega$. On the other hand, let $y \in \Omega$. Since 0 is in the interior for Ω , there exists $\lambda \geq 1$ such that $\tilde{y} := \lambda y \in \partial\Omega$. Hence, there exists $\tilde{x} \in \partial B$ s.t. $\tilde{y} = \nabla h_\Omega(\tilde{x})$. By taking $x = \frac{1}{\lambda}\tilde{x} \in B$, we have $y = \|x\|\nabla h(x)$. Hence $\tilde{\Omega} = \Omega$, meaning that $\phi(B)$ is convex.

One must now prove the injectivity of ϕ . Let $x_1, x_2 \in \mathbb{R}^d \setminus \{0\}$ be such that $\phi(x_1) = \phi(x_2)$. Hence, $\nabla h(x_1)$ and $\nabla h(x_2)$ are positively colinear. Moreover, $\nabla h(x_1), \nabla h(x_2) \in \partial\Omega$. However, since $h > 0$, we have that $0 \in \text{int}(\Omega)$. Hence, any half line originating at 0 must intersect $\partial\Omega$ exactly once (by convexity), implying that $\nabla h(x_1) = \nabla h(x_2)$ and further $\|x_1\| = \|x_2\|$. Using that $\nabla h : \mathbb{S}^{n-1} \rightarrow \partial\Omega$ is a homeomorphism, this means that $\frac{x_1}{\|x_1\|} = \frac{x_2}{\|x_2\|}$ and hence $x_1 = x_2$. \square

2.2 Sublinear neural networks

In what follows, we parametrize convex sets *via* their gauge or support function. To this end, we will construct a neural network $p_\theta : \mathbb{R}^d \rightarrow \mathbb{R}$, with parameters θ , that is sublinear by design.

A natural starting point is the MaxOut layer [21], defined as $p_\theta(x) = \max_{1 \leq i \leq N}(w_i \cdot x)$, where $w_i \in \mathbb{R}^d$. This choice is motivated by the classical characterization of sublinear functions as point-wise supremum of linear forms. However, this representation is non-smooth, which can be limiting in applications requiring differential quantities such as normals or curvature, or even for the application of Proposition 2.2. To address this, we could consider to replace the maximum by a smooth approximation, like the LogSumExp (LSE). Unfortunately, the obtained function would not be sublinear anymore. Nevertheless, we are able to recover sublinearity while preserving the trace on the sphere as we will see hereafter. This requires classical tools from convex analysis, that we recall in Section A for completeness.

Proposition 2.3. *Let $f : \mathbb{R}^d \rightarrow (-\infty, +\infty]$ be a proper convex and closed function such that $f^* \leq 0$ on its domain. Let $x \in \mathbb{R}^d$ and define*

$$h(x) := \|x\|f\left(\frac{x}{\|x\|}\right)$$

with $h(0) := 0$. Then h is sublinear.

Proof. First, h is positively homogeneous by construction. Hence, sublinearity is equivalent to convexity, and we will show the latter. According Proposition A.1, we can write

$$f(x) = f^{**}(x) = \sup_{y \in \text{dom}(f^*)} \{y \cdot x - f^*(y)\},$$

which leads to $h(x) = \sup_{y \in \text{dom}(f^*)} \{y \cdot x - \|x\|f^*(y)\}$. Since $f^* \leq 0$ on its domain, the function $x \mapsto y \cdot x - \|x\|f^*(y)$ is convex, implying that h is convex as the supremum of a family of convex functions. \square

Using the previous proposition, we can finally define our Neural Network as

$$p_\theta(x) := \beta\|x\|\text{LSE}\left(W^T \frac{x}{\|x\|}\right) \quad \text{where} \quad \text{LSE}(y_1, \dots, y_n) = \log\left(\sum_{i=1}^n e^{y_i}\right). \quad (2)$$

Proposition 2.4. p_θ as defined in Eq. (2) is a sublinear function which is C^∞ on $\mathbb{R}^d \setminus \{0\}$.

Proof. The regularity assumption is obvious. Since the LSE is a convex function with values in \mathbb{R} , it is proper and closed. The sublinearity can be shown as follows: let $f(x) = \text{LSE}(W^T x)$. According to Proposition 2.3, it is enough to show that f^* is non positive. According to Proposition A.3 and Proposition A.2, we have that

$$f^*(y) \leq W \triangleright (-S)(y) = \inf_{Wx=y} -S(x) \leq 0$$

where S is the entropy function defined in Proposition A.3. □

Remark 2.1. According to the previous derivations, one does not need to restrict to the LSE activation function. Indeed, any convex function such that $f^* \leq 0$ on its domain would also give rise to a sublinear network. The proof of the universal approximation property (given hereafter) however heavily depends on the fact that the LSE approximates the maximum function.

Remark 2.2. One might ask whether this construction can be extended to deeper networks. However, such a generalization is not straightforward, due to the complex interaction between convex conjugation and function composition.

2.3 Universal approximation

According to Proposition 2.1 and Proposition 2.2, the neural networks

$$\phi_\theta(x) := \frac{\|x\|}{p_\theta(x)} x \tag{3}$$

and

$$\phi_\theta(x) := \|x\| \nabla p_\theta(x) \tag{4}$$

define convex sets by $\Omega_\theta := \phi_\theta(B)$ where p_θ is respectively the gauge or support function (see Fig. 1 for an illustration of the action of these maps on the unit ball). However, it is of core interest to know whether every convex set can be represented using this architecture. It turns out that we have the following universal approximation property:

Theorem 2.1. Let $\mathcal{K}^{NN} := \{\Omega_\theta \subset \mathbb{R}^d : \beta > 0, W \in \mathbb{R}^{d \times m}, m \in \mathbb{N}\}$ be the set of convex set that can be represented by Eq. (3) or Eq. (4). Then \mathcal{K}^{NN} is dense in \mathcal{K} with respect to the Hausdorff distance.

Sketch of proof. Let $\Omega \subset \mathcal{K}$. We can approximate this set, in the Hausdorff sense, by a polyhedron $P := \bigcap_{1 \leq i \leq m} \{x \in \mathbb{R}^d : w_i \cdot x \leq 1\}$. The gauge function of this polyhedron is $g_P(x) = \max_{1 \leq i \leq m} w_i \cdot x$, which can be approximated by a sublinear network p_θ using the property of the LSE to approximate the maximum function. The corresponding Ω_θ can be made as close to P as desired, hence close to Ω .

The case of the parametrization by a support function is done in a similar way, by observing that the support function of a polytope $P = \text{Conv}(p_1, \dots, p_n)$ is $h_P(x) = \max\{p_1 \cdot x, \dots, p_n \cdot x\}$.

The full proof is provided in Section B. □

Symmetries A natural question is to know whether we can enforce symmetries on the parametrized shapes. In term of group actions, it amounts at asking if, for a certain group of symmetries G we can make Ω invariant with respect to the action of G , i.e. $g \cdot \Omega = \Omega$ for all $g \in G$. In our case, we achieve invariance by *frame averaging* [22]. Given G a finite subgroup of isometries of \mathbb{R}^d and p_θ a sublinear network, we define $p_\theta^G(x) := \frac{1}{|G|} \sum_{g \in G} p_\theta(g \cdot x)$. we have the following proposition:

Proposition 2.5. Let p_θ^G be either the gauge or support function of a convex set Ω_θ . Then Ω_θ is invariant with respect to G .

The proof of this proposition is provided in Section B. An experiment making use of the symmetries of both the gauge and support functions can be found in Section E.

3 Computation of shape quantities

Shape optimization problems, as well as certain inverse problems, require to optimize a certain criteria involving quantities related to the shape, like the volume, perimeter, curvature, etc, for which we can benefit from automatic differentiation. Note that various other quantities are studied in [23].

3.1 Integral quantities

We pull back the computations to the reference domain, using change of variables [24]:

$$\int_{\Omega_\theta} f dx = \int_B (f \circ \phi_\theta) \text{Jac}(\phi_\theta) dx \quad \text{and} \quad \int_{\partial\Omega_\theta} g d\sigma = \int_{\partial B} (g \circ \phi_\theta) \text{Jac}_{\partial B}(\phi_\theta) d\sigma,$$

where $\text{Jac}(\phi_\theta) = |\det(D\phi_\theta)|$, $\text{Jac}_{\partial B}(\phi_\theta) = \text{Jac}(\phi_\theta) \| (D\phi_\theta)^{-T} n_B \|$ and $n_B(x) := x$ on ∂B is the unit outward normal vector. For instance, we can compute the volume and perimeter (i.e. surface area) of Ω_θ as $\text{Vol}(\Omega_\theta) = \int_B \text{Jac}\phi_\theta dx$ and $\text{Per}(\Omega_\theta) = \int_{\partial B} \text{Jac}_{\partial B}(\phi_\theta) d\sigma$. All the differential quantities are automatically computed using PyTorch [25]. The integrals can be discretized using either Monte-Carlo or fixed quadrature points. We chose the latter approach, as we will mainly use L-BFGS as an optimizer, which is known for being sensitive to noise. In particular, we use a Fibonacci lattice approach for the discretizations on the 2-sphere [26].

3.2 Geometric-differential quantities

Let $y = \phi_\theta(x)$, $x \in \partial B$. We can express the normal vector at $y \in \partial\Omega_\theta$ by

$$n_\theta(y) = \frac{(D\phi_\theta)^{-T}(x)n_B(x)}{\|(D\phi_\theta)^{-T}(x)n_B(x)\|}.$$

This naturally defines an extended vector field in $\mathbb{R}^d \setminus \{0\}$. The mean curvature and Gaussian curvature are respectively defined as

$$H_\theta(y) = (d-1)^{-1} \text{tr} S_y \quad \text{and} \quad \kappa_\theta(y) = \det S_y$$

where S_y is the *Weingarten map* at y . For more details, see Section C.1.

3.3 PDE-related quantities

It is common in shape optimization to consider quantities that depends on the solution of a PDE. For instance, optimal design of structures often minimize for the compliance, which is a by-product of the linear elasticity equation; aerodynamic shape optimization needs to solve Navier-Stokes. In this section, we show how it is possible to seamlessly bridge precise and robust mesh free methods with the auto-differentiation of PyTorch in order to easily compute derivatives of PDE-dependent quantities in the simple case of the Poisson equation.

Mesh free Galerkin method: For $f \in L^2(\Omega_\theta)$, the Poisson problem with Dirichlet boundary condition aims at finding $u \in H_0^1(\Omega_\theta)$ which satisfies

$$\begin{cases} -\Delta u = f & \text{in } \Omega_\theta, \\ u = 0 & \text{on } \partial\Omega_\theta. \end{cases} \quad (5)$$

Passing to the *weak formulation* [27] and changing variables, Eq. (5) can be express in a weak sense as

$$\int_B A_\theta \nabla u \cdot \nabla v = \int_B (\text{Jac}\phi_\theta)(f \circ \phi_\theta)v,$$

for $u, v \in H_0^1(B)$, where $A_\theta := (\text{Jac}\phi_\theta)(D\phi_\theta)^{-1}(D\phi_\theta)^{-T}$. The Dirichlet boundary condition is weakly enforced by adding a penalization term with penalty parameter $\alpha > 0$. The resulting problem is then discretized on a subspace spanned by radial basis functions (RBFs) $\varphi_i(x) := \psi(|x - x_i|)$, $x_i \in B$, possibly augmented by a polynomial basis [28] leading to a system $K\bar{u} = \bar{f}$, where

$$K_{ij} = \int_B A_\theta \nabla \varphi_i \cdot \nabla \varphi_j + \alpha \int_{\partial B} \varphi_i \varphi_j \quad \text{and} \quad \bar{f}_i = \int_B (\text{Jac}\phi_\theta)(f \circ \phi_\theta) \varphi_i.$$

The integrals are discretized as previously described. We can then solve the previous linear system and recover the solution $u(x) = \sum_i \bar{u}_i \varphi_i(x)$.

Remark 3.1. *The RBF-Galerkin method is chosen because of its theoretical convergence guarantees (unlike other meshless methods relying on the strong formulation of the PDE like the Kansa method [29] or PINN-based methods [30]) and is easy to implement in PyTorch.*

Method of fundamental solutions An important particular case of Eq. (5) is for $f = 1$, in which case the equation can be solved thanks to a method exhibiting spectral convergence. The details are provided in Section C.2.

A note on the use of PINNs One may wonder why we do not use PINNs to solve the PDEs, as in related work [14]. Our choice is guided by both practical and structural considerations. On the practical side, recent studies indicate that PINNs do not match the efficiency of classical solvers on several low-dimensional PDEs [31, 32], which is confirmed by our experiments. On the structural side, while [14] relies on a min–min formulation enabling joint optimization, most shape optimization problems are naturally min–max, requiring the inner problem to be (approximately) solved at each step, which increases computational cost.

For completeness, we include a comparison with PINNs in Section D, where classical methods remain way more efficient in our setting.

On shape derivatives and the FEM Classical approaches to minimizing a shape functional J rely on shape derivatives evaluated on a mesh. Their numerical implementation typically involves additional components such as adjoint states and extension–regularization procedures, which require solving PDEs on the domain. In contrast, our approach avoids these steps by leveraging automatic differentiation.

That said, mesh-based methods remain highly accurate and may be desirable in this context. However, there is currently no standard PyTorch-based framework for finite element computations. We discuss a possible interface with external FEM libraries in Section G.

3.4 Which representation should be used?

In most cases, the gauge and support functions representations are interchangeable, since computations of shape quantities only rely on the fact that ϕ_θ is a smooth bijection and not on its particular structure. However, there is certain cases where one of the parametrization is preferable, like the gauge parametrization in Section 4.1 or the support parametrization in Section 4.4. The gauge parametrization may also be preferred when one needs an explicit inverse, as illustrated in Section G. Moreover, certain geometric quantities that we do not discuss here are easier to compute with a certain representation (for instance, the *width* is easily computed in the support function parametrization).

Remark 3.2. *Notably, the arguments in this section do not rely on the convexity of Ω_θ or on any special structure of ϕ_θ . This suggests that the framework can be extended beyond the present setting to arbitrary invertible neural networks ϕ_θ , which we leave to future work.*

4 Application to shape optimization problems

In this section, we present the performance of our method on a range of problems arising from geometry and shape optimization. For fairness and reproducibility, all experiments are conducted on a single CPU (AMD Ryzen 7 Pro) with 28 GB of RAM. The computational time for all two-dimensional cases is on the order of one minute, while in three dimensions it is typically on the order of ten minutes. The implementation is also CUDA-compatible and can therefore benefit from standard GPU acceleration. A direct quantitative comparison with classical methods is not possible in practice, as no publicly available implementations exist in a form that would allow a consistent and reproducible evaluation.

4.1 Learning convex sets with noisy boundary samples

The first problem we consider is to reconstruct a convex shape from noisy observations. More precisely, given sampled $y_1, \dots, y_n \in \mathbb{R}^d$, we minimize $L(\theta) = \sum_{i=1}^n |p_\theta(y_i) - 1|^2$ where p_θ is the gauge function of the convex set Ω_θ . This loss is motivated by the fact that $\partial\Omega_\theta = \{p_\theta = 1\}$.

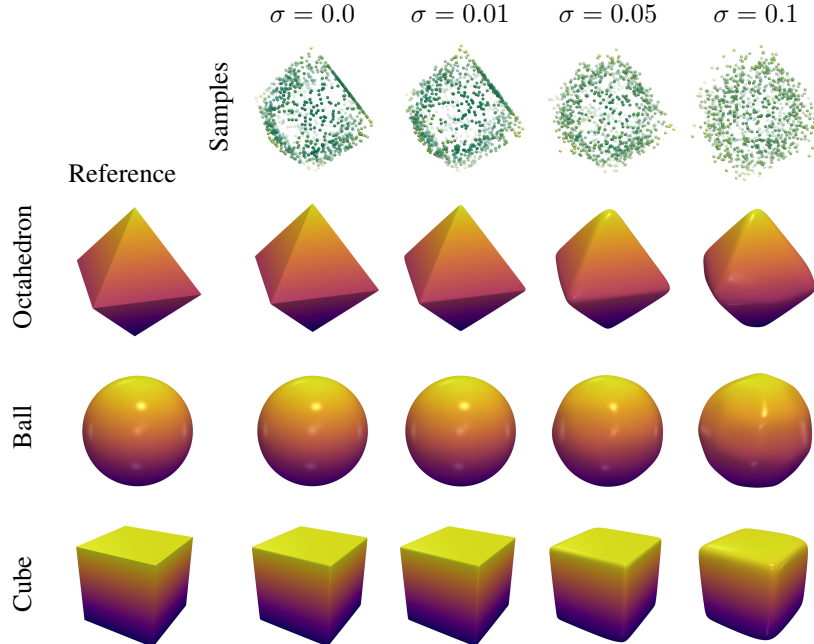


Figure 2: Reconstruction of convex shapes from noisy point clouds. First column: reference shapes. Top row: input point clouds sampled from the octahedron under increasing Gaussian noise levels σ . Remaining rows: reconstructed shapes for different target geometries.

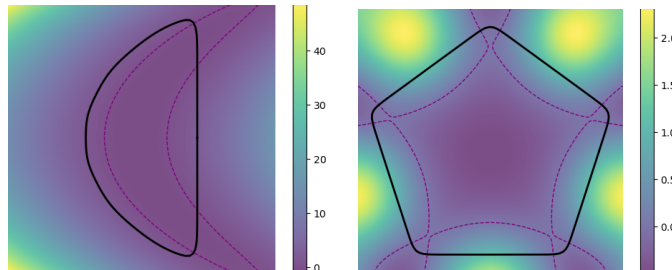


Figure 3: Optimal shape for the Poisson-based shape optimization problem (in black) along with the function f . The dotted line is the 0 level set.

In practice, the observations y_i are generated synthetically as follows: first, $x_i \sim \mathcal{U}(\partial B)$. Then, $y_i = \phi_{\text{target}}(x_i) + \varepsilon_i$ where $\varepsilon_i \sim \mathcal{N}(0, \sigma)$, and ϕ_{target} denotes a maps from B to Ω_{target} . The results, shown in Fig. 2, are obtained with $n = 1000$ samples and varying noise levels across three different shapes. We observe that the convex inductive bias enables an accurate reconstruction of the shapes, even with a relatively small number of samples and substantial noise. Additional statistical experiments assessing sensitivity to noise and to the amount of samples over multiple runs are reported in Section F.

4.2 Optimization of a Poisson problem

One of the simplest PDE-constrained shape optimization problem is the following: considering a function $f : \mathbb{R}^d \rightarrow \mathbb{R}$ and u_θ to be the solution of Eq. (5) on a domain $\Omega_\theta \in \mathcal{K}$, what is the minimum of $J(\Omega_\theta) := \int_{\Omega_\theta} u_\theta$? As described previously, the solution u_θ is computed by a mesh free Galerkin method, while the integral is evaluated by change of variables. We performs our experiments in the same settings as in [7], i.e. in dimension 2 for two different functions f . The optimal shapes are given in Fig. 3. They can be compared to the ones in [7].

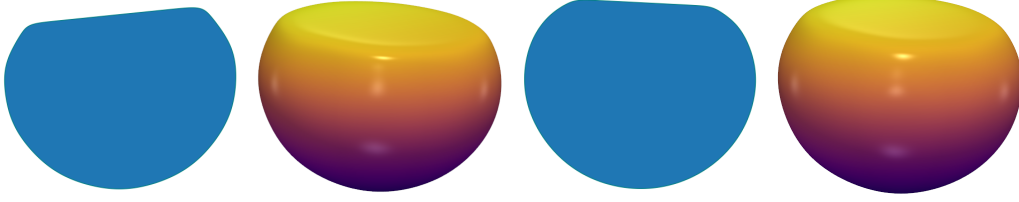


Figure 4: Optimal shapes for maximizing the torsion gradient under two constraints: fixed volume (left) and fixed perimeter (right). While the resulting shapes are similar, the choice of normalization produces distinct geometries.

Table 1: Optimal values for J_{Vol} and J_{Per} in several dimensions.

Dimension	J_{Vol}^*	J_{Per}^*
2	0.35809	0.09886
3	0.30918	0.13842
4	0.28397	0.15532

4.3 Maximization of the gradient of the torsion function

In linear elasticity, the quantity $\|\nabla u_{\Omega}\|_{L^{\infty}}$ (where u_{Ω} is the torsion function Eq. (7)) represents the maximal shear stress of a rod with section Ω . In the case of a planar convex domain $\Omega \subset \mathbb{R}^d$, many authors were interested in knowing what shape maximized this quantity when prescribing the area or the perimeter (see [33] and references therein). Using homogeneity arguments, it amounts at maximizing respectively $\frac{\|\nabla u_{\Omega}\|_{L^{\infty}}}{\text{Vol}(\Omega)^{1/d}}$ and $\frac{\|\nabla u_{\Omega}\|_{L^{\infty}}}{\text{Per}(\Omega)^{1/(d-1)}}$. Assuming enough regularity, the maximum principle applied on $|\nabla u|^2$ ensures that the infinity norm is attained on the boundary, i.e. $\|\nabla u_{\Omega}\|_{L^{\infty}} = \max_{\partial\Omega} |\partial_n u|$. For a parametrized convex set Ω_{θ} , maximizing the previous quantities is hence equivalent to maximizing respectively

$$J_{\text{Vol}}(\theta) := \frac{|\partial_n u_{\Omega_{\theta}}(\phi_{\theta}(x))|}{\text{Vol}(\Omega_{\theta})^{1/d}} \quad \text{and} \quad J_{\text{Per}}(\theta) := \frac{|\partial_n u_{\Omega_{\theta}}(\phi_{\theta}(x))|}{\text{Per}(\Omega_{\theta})^{1/(d-1)}}.$$

for a fixed $x \in \partial B$. The optimal shapes in dimension 2 and 3 are given in Fig. 4. In order to show that our algorithm easily adapts to higher dimensions, we give in Table 1 the optimal values obtained with our method for each functionals in dimension up to 4. In dimension 2, the values that are obtained matches previous numerical experiments found in the literature [33].

4.4 Minkowski problem

The Minkowski problem [34] is a foundational problem in convex and differential geometry, connected to the famous Monge–Ampère equation. Informally speaking, it is concerned with the question of existence of a convex set with prescribed Gaussian curvature. More precisely, let $g : \mathbb{S}^{n-1} \rightarrow \mathbb{R}$ be a positive, continuous function. Does there exists a convex set Ω such that $\kappa_{\Omega} \circ n_{\Omega}^{-1} = g$ on ∂B ? It is known that such Ω exists if and only if g verifies $\int_{\partial B} \frac{u}{g(u)} du = 0$. We can approximate this problem by formulating it as a regression problem, by minimizing the relative mean squared error between the actual and target curvature:

$$L(\theta) = \int_{\partial B} \left| \frac{\kappa_{\theta}(n_{\theta}^{-1}(u)) - g(u)}{g(u)} \right|^2 du.$$

Except for n_{θ}^{-1} , everything is easily computable in the present framework. However, as it is pointed out in [20], if p_{θ} is the support function of Ω_{θ} (i.e., choosing the parametrization Eq. (4)) we have $n_{\theta}^{-1} = \nabla p_{\theta} = \phi_{\theta}$ on ∂B . Hence, the previous loss is readily computable. We show that our method successfully applies to the Minkowski problem in Fig. 5. The final L^2 relative error is of the order of 10^{-2} .

Reproducibility The code is fully available on GitHub: <https://anonymous.4open.science/r/SublinearNet-5726/>.

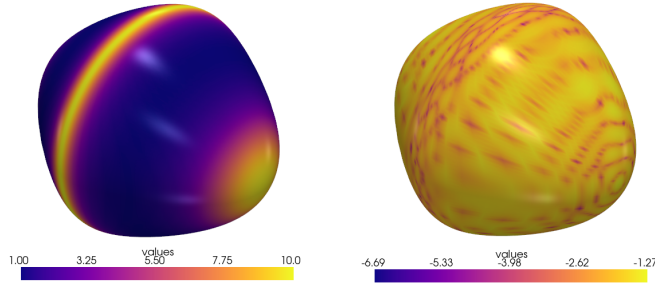


Figure 5: Solution to the Minkowski problem. Left: prescribed curvature. Right: \log_{10} relative error. The method accurately recovers the target curvature distribution.

5 Discussion

The proposed approach allows for a provably expressive and unconstrained representation of convex sets. Profiting from the auto-differentiation capabilities of PyTorch, it allows to easily solve a large variety of shape optimization problems without any shape derivative computation.

Limitations However, several limitations remain. The reliance on quasi-Newton methods like L-BFGS with fixed discretizations limits scalability due to the curse of dimensionality. Certain geometric quantities (e.g., curvature) may become unstable near non-smooth shapes. Memory usage is also higher than in classical approaches, since PDE solvers must remain in the computational graph. Finally, symmetry enforcement increases computational cost linearly with respect to the size of the symmetry group due to repeated evaluations.

Broader impact We validate the proposed method primarily on mathematical shape optimization problems, where it may help accelerate exploration and conjecture generation. Extending the framework to more realistic engineering settings—such as structural or aerodynamic optimization—could further broaden its applicability and impact.

6 Conclusion

We introduced a neural parametrization of convex sets based on sublinear networks, ensuring exact convexity while retaining strong approximation capabilities. We proved universal approximation in the Hausdorff distance and showed how the parametrization enables efficient evaluation of geometric and PDE-dependent quantities via automatic differentiation.

Numerical experiments demonstrate competitive performance on a range of shape optimization problems, and show that classical solvers combined with our parametrization outperform PINN-based approaches in both accuracy and efficiency.

Future work includes extending the framework to more complex PDEs (e.g., elasticity or fluid dynamics) and designing architectures that preserve additional geometric constraints, like the volume (using measure-preserving neural networks) or the perimeter, for which a new architecture must probably be derived.

Acknowledgments

Large language models were used to assist with code generation—particularly for plotting—and to explore mathematical ideas.

References

- [1] Giuseppe Buttazzo and Paolo Guasoni. Shape optimization problems over classes of convex domains. *Journal of Convex Analysis*, 4:343–352, 1997.

- [2] Édouard Oudet. Numerical minimization of eigenmodes of a membrane with respect to the domain. *ESAIM Control Optim. Calc. Var.*, 10(3):315–330, 2004.
- [3] Thomas Lachand-Robert and Édouard Oudet. Minimizing within Convex Bodies Using a Convex Hull Method. *SIAM J. Optim.*, 2006.
- [4] Édouard Oudet. Shape Optimization Under Width Constraint. *Discrete Comput. Geom.*, 49(2): 411–428, 2013.
- [5] Pedro R. S. Antunes and Benjamin Bogosel. Parametric shape optimization using the support function. *Comput. Optim. Appl.*, 82(1):107–138, 2022.
- [6] T erence Bayen and Didier Henrion. Semidefinite programming for optimizing convex bodies under width constraints. *Optim. Methods Softw.*, 2012.
- [7] Benjamin Bogosel. Numerical Shape Optimization Among Convex Sets. *Appl. Math. Optim.*, 87(1):1, 2023.
- [8] Benjamin Bogosel, Antoine Henrot, and Marco Michetti. Optimization of Neumann Eigenvalues Under Convexity and Geometric Constraints. *SIAM J. Math. Anal.*, November 2024.
- [9] Ilias Ftouhi. Improved Description of Blaschke–Santal o Diagrams via Numerical Shape Optimization. *Appl. Math. Optim.*, 91(3):55, 2025.
- [10] L Lamberg and M Kaasalainen. Numerical solution of the minkowski problem. *Journal of computational and applied mathematics*, 137(2):213–227, 2001.
- [11] S oren Bartels and Gerd Wachsmuth. Numerical Approximation of Optimal Convex Shapes. *SIAM J. Sci. Comput.*, April 2020.
- [12] Abdelkrim Chakib, Ibrahim Khalil, and Azeddine Sadik. An improved numerical approach for solving shape optimization problems on convex domains. *Numerical Algorithms*, 96(2): 621–663, 2024.
- [13] Seungyeon Shin, Dongju Shin, and Namwoo Kang. Topology optimization via machine learning and deep learning: a review. *Journal of Computational Design and Engineering*, 10(4): 1736–1766, 2023.
- [14] Amaury B eli eres Frendo, Emmanuel Franck, Victor Michel-Dansac, and Yannick Privat. Volume-preserving geometric shape optimization of the Dirichlet energy using variational neural networks. *Neural Networks*, 184:106957, 2025.
- [15] Eloi Martinet and Leon Bungert. Meshless Shape Optimization Using Neural Networks and Partial Differential Equations on Graphs. In *Scale Space and Variational Methods in Computer Vision*, pages 285–297. 2025.
- [16] Brandon Amos, Lei Xu, and J. Zico Kolter. Input convex neural networks. In *International Conference on Machine Learning (ICML)*, 2017.
- [17] Jun Liu, Kehui Zhang, Xue-Cheng Tai, and Shousheng Luo. Convex shape prior for deep convolution neural network-based image segmentation. *Journal of Mathematical Imaging and Vision*, 67(6):61, 2025.
- [18] B. Deng, K. Genova, S. Yazdani, S. Bouaziz, G. Hinton, and A. Tagliasacchi. Cvxnet: Learnable convex decomposition. In *Proceedings of the IEEE/CVF Conference on Computer Vision and Pattern Recognition (CVPR)*, 2020.
- [19] Lenka T etkova, Thea Br usch, Teresa Dorszewski, Fabian Martin Mager, Rasmus  rtoft Aagaard, Jonathan Foldager, Tommy Sonne Alstr om, and Lars Kai Hansen. On convex decision regions in deep network representations. *Nature Communications*, 16(1):5419, 2025.
- [20] R. Schneider. *Convex Bodies: The Brunn-Minkowski Theory*. Cambridge University Press, 2nd expanded edition, 2013.

- [21] Ian Goodfellow, David Warde-Farley, Mehdi Mirza, Aaron Courville, and Yoshua Bengio. Maxout networks. In *International conference on machine learning*, pages 1319–1327. PMLR, 2013.
- [22] Omri Puny, Matan Atzmon, Heli Ben-Hamu, Ishan Misra, Aditya Grover, Edward J Smith, and Yaron Lipman. Frame averaging for invariant and equivariant network design. *arXiv preprint arXiv:2110.03336*, 2021.
- [23] Eloi Martinet and Ilias Ftouhi. Numerical exploration of the range of shape functionals using neural networks. *arXiv preprint arXiv:2602.14881*, 2026.
- [24] Lawrence C Evans. *Measure theory and fine properties of functions*. 2025.
- [25] Adam Paszke, Sam Gross, Francisco Massa, Adam Lerer, James Bradbury, Gregory Chanan, Trevor Killeen, Zeming Lin, Natalia Gimelshein, Luca Antiga, et al. Pytorch: An imperative style, high-performance deep learning library. *Advances in neural information processing systems*, 32, 2019.
- [26] Álvaro González. Measurement of Areas on a Sphere Using Fibonacci and Latitude–Longitude Lattices. *Math. Geosci.*, 42(1):49–64, 2010.
- [27] Lawrence C Evans. *Partial differential equations*, volume 19. 2022.
- [28] Holger Wendland. Meshless galerkin methods using radial basis functions. *Mathematics of Computation*, 68(228):1521–1531, 1999.
- [29] Gregory E Fasshauer. *Meshfree approximation methods with Matlab (With Cd-rom)*, volume 6. World Scientific Publishing Company, 2007.
- [30] MWM Gamini Dissanayake and Nhan Phan-Thien. Neural-network-based approximations for solving partial differential equations. *communications in Numerical Methods in Engineering*, 10(3):195–201, 1994.
- [31] Tamara G Grossmann, Urszula Julia Komorowska, Jonas Latz, and Carola-Bibiane Schönlieb. Can physics-informed neural networks beat the finite element method? *IMA Journal of Applied Mathematics*, 89(1):143–174, 2024.
- [32] Nick McGreivy and Ammar Hakim. Weak baselines and reporting biases lead to overoptimism in machine learning for fluid-related partial differential equations. *Nature machine intelligence*, 6(10):1256–1269, 2024.
- [33] Krzysztof Burdzy, Ilias Ftouhi, and Phanuel Mariano. Geometric properties of optimizers for the maximum gradient of the torsion function. *arXiv preprint arXiv:2512.09400*, 2025.
- [34] Yong Huang, Deane Yang, and Gaoyong Zhang. Minkowski problems for geometric measures. *Bulletin of the American Mathematical Society*, 62(3):359–425, 2025.
- [35] Stephen P Boyd and Lieven Vandenbergh. *Convex optimization*. Cambridge university press, 2004.
- [36] Heinz H Bauschke and Patrick L Combettes. Correction to: convex analysis and monotone operator theory in hilbert spaces. In *Convex analysis and monotone operator theory in Hilbert spaces*. Springer, 2020.
- [37] Alex H Barnett and Timo Betcke. Stability and convergence of the method of fundamental solutions for helmholtz problems on analytic domains. *Journal of Computational Physics*, 227(14):7003–7026, 2008.
- [38] Beniamin Bogosel. The method of fundamental solutions applied to boundary eigenvalue problems. *J. Comput. Appl. Math.*, 306:265–285, 2016.
- [39] Liviu Marin and Daniel Lesnic. The method of fundamental solutions for the cauchy problem in two-dimensional linear elasticity. *International journal of solids and structures*, 41(13):3425–3438, 2004.

- [40] Carlos JS Alves, Rodrigo G Serrao, and Ana L Silvestre. Fundamental solutions for the stokes equations: Numerical applications for 2d and 3d flows. *Applied Numerical Mathematics*, 170: 55–73, 2021.
- [41] Lorenzo Brasco and Guido De Philippis. Spectral inequalities in quantitative form. *arXiv preprint arXiv:1604.05072*, 2016.
- [42] Bing Yu et al. The deep ritz method: a deep learning-based numerical algorithm for solving variational problems. *Communications in Mathematics and Statistics*, 6(1):1–12, 2018.
- [43] Nicola Fusco, Francesco Maggi, and Aldo Pratelli. The sharp quantitative isoperimetric inequality. *Annals of mathematics*, pages 941–980, 2008.
- [44] K Böröczky, E Makai, Mathieu Meyer, and Shlomo Reisner. On the volume product of planar polar convex bodies—lower estimates with stability. *Studia Scientiarum Mathematicarum Hungarica*, 50(2):159–198, 2013.
- [45] Antoine Henrot and Michel Pierre. *Shape variation and optimization*, volume 28 of *EMS Tracts in Mathematics*. European Mathematical Society (EMS), Zürich, 2018.
- [46] Christophe Geuzaine and Jean-François Remacle. Gmsh: A 3-d finite element mesh generator with built-in pre-and post-processing facilities. *International journal for numerical methods in engineering*, 79(11):1309–1331, 2009.
- [47] Tom Gustafsson and Geordie Drummond Mcbain. scikit-fem: A python package for finite element assembly. *Journal of Open Source Software*, 5(52):2369, 2020.

A Reminder of convex analysis

Here we give some useful results of convex analysis. We begin with the definition of the convex conjugate of a function, that can be found in [35].

Definition A.1 (Convex conjugate). *Let $f : \mathbb{R}^d \rightarrow (-\infty, +\infty]$. The convex conjugate of $f^* : \mathbb{R}^d \rightarrow (-\infty, +\infty]$ is defined as*

$$f^*(y) := \sup_{x \in \text{dom}(f)} \{y \cdot x - f(x)\} \quad (6)$$

where $\text{dom}(f)$ is the set of $x \in \mathbb{R}^d$ such that $f(x) < +\infty$.

The following proposition can be found in [35, Exercise 3.39]:

Proposition A.1. *Let $f : \mathbb{R}^d \rightarrow [-\infty, +\infty]$ be a proper convex and closed function. Then $f^{**} = f$.*

In what follows, it will be useful to compute the composition of a convex function with a linear layer. The behavior of the convex conjugate with respect to the composition needs the following definition [36, Definition 12.34]:

Definition A.2 (Infimal postcomposition). *Let $f : \mathbb{R}^d \rightarrow [-\infty, +\infty]$ and $L : \mathbb{R}^d \rightarrow \mathbb{R}^m$. The infimal postcomposition of f by L is*

$$L \triangleright f : \mathbb{R}^m \longrightarrow [-\infty, +\infty] \\ y \longmapsto \inf_{Lx=y} f(x)$$

In our case, we will only need the conjugate of the composition with a linear map, which is given by the following proposition (adapted from [36, Proposition 13.24]):

Proposition A.2 (Composition with a linear map). *Let $f : \mathbb{R}^d \rightarrow (-\infty, +\infty]$ and $A \in \mathbb{R}^{n \times m}$. Then*

$$(f \circ A)^* \leq A^T \triangleright f^*.$$

Finally, we will need to know the conjugate of the log-sum-exp function:

Proposition A.3 (Convex conjugate of the log-sum-exp). *The convex conjugate of the log-sum-exp is the negative entropy function $-S$ where*

$$\begin{aligned} S: \Delta^N &\longrightarrow (0, +\infty) \\ y &\longmapsto -\sum_i y_i \log y_i \end{aligned}$$

where Δ^N is the N -dimensional simplex.

This can be shown by computing the optimality conditions in (6) (see [35, Example 3.25] for more details).

B Proofs

Proof of Theorem 2.1. We need to split the cases according to the definition of Ω_θ . First, we define for $K, L \in \mathcal{K}$ the Hausdorff distance as $d_H(K, L) := \sup\{\sup_{x \in K} d(x, L), \sup_{x \in L} d(x, K)\}$.

Support function case: Let $K \in \mathcal{K}$, $\varepsilon > 0$. According to [20, Theorem 1.8.19], there exist a polytope $P = \text{Conv}(w_1, \dots, w_m)$ such that $d_H(K, P) \leq \varepsilon/2$. It is well known that the support function of p is given by $h_P(x) := \sup_{1 \leq i \leq m} w_i \cdot x$. Now, let p_θ as defined in Eq. (2) be such that $\theta = \{\beta, W_\beta\}$ where $W_\beta := \beta^{-1}(w_1 \dots w_m)^T$ and let Ω_θ be defined by Eq. (4). This implies in particular that $h_{\Omega_\theta} = p_\theta$. Since the log-sum-exp approximates the maximum function, we can take β small enough so that $\|h_P - p_\theta\|_{C(\mathbb{S}^{n-1})} \leq \varepsilon/2$. Moreover, according to [20, Lemma 1.8.14], $d_H(P, \Omega_\theta) = \|h_P - p_\theta\|_{C(\mathbb{S}^{n-1})}$. Putting everything together, we get that there exists θ such that

$$d_H(K, \Omega_\theta) \leq d_H(K, P) + d_H(P, \Omega_\theta) \leq \varepsilon$$

hence \mathcal{K}^{NN} is dense in \mathcal{K} .

Gauge function case: We first prove the following fact: for $K, L \in \mathcal{K}$, we have $d_H(K, L) \leq \|\rho_K - \rho_L\|_{C(\mathbb{S}^{n-1})}$ where

$$\begin{aligned} \rho_K: \mathbb{S}^{n-1} &\longrightarrow \mathbb{R}^+ \\ x &\longmapsto \sup\{r > 0 : rx \in K\} \end{aligned}$$

is the *radial function* of K . In particular, it is immediate that the radial function is the inverse of the gauge function on \mathbb{S}^{n-1} . For $x \in K$, let us define

$$y = \begin{cases} \rho_L \left(\frac{x}{\|x\|} \right) \frac{x}{\|x\|} & \text{if } x \notin L \\ x & \text{if } x \in L \end{cases}.$$

Then $y \in L$ and we have

$$d(x, L) \leq \max \left\{ 0, \|x\| - \rho_L \left(\frac{x}{\|x\|} \right) \right\} \leq \left| \rho_K \left(\frac{x}{\|x\|} \right) - \rho_L \left(\frac{x}{\|x\|} \right) \right| \leq \|\rho_K - \rho_L\|_{C(\mathbb{S}^{n-1})}$$

Hence $\sup_{x \in K} d(x, L) \leq \|\rho_K - \rho_L\|_{C(\mathbb{S}^{n-1})}$. By symmetry, we deduce the claim.

Now, let $K \in \mathcal{K}$, $\varepsilon > 0$. Let P be a polytope such that $P \subset K$ and $d_H(K, P) \leq \varepsilon$. According to [20, Theorem 2.4.3], there exists $m > 0$ and vectors $w_1, \dots, w_m \in \mathbb{R}^d$ such that

$$P := \bigcap_{1 \leq i \leq m} \{x \in \mathbb{R}^d : w_i \cdot x \leq 1\}.$$

In particular, we have $g_P(x) = \max_{1 \leq i \leq m} w_i \cdot x$. The condition $P \subset K$ implies that $0 < \alpha := \min_{u \in \mathbb{S}^{n-1}} g_K(u) \leq \min_{u \in \mathbb{S}^{n-1}} g_P(u)$. Similarly as before, we can take β small enough so that

$$\|g_P - p_\theta\|_{C(\mathbb{S}^{n-1})} \leq \varepsilon \quad \text{and} \quad \min_{u \in \mathbb{S}^{n-1}} p_\theta(u) \geq \alpha/2.$$

Hence, for Ω_θ defined as in Eq. (3), we have

$$\|\rho_{\Omega_\theta} - \rho_P\|_{C(\mathbb{S}^{n-1})} = \left\| \frac{1}{p_\theta} - \frac{1}{g_P} \right\|_{C(\mathbb{S}^{n-1})} \leq \frac{\varepsilon}{\min_{\mathbb{S}^{n-1}} p_\theta \min_{\mathbb{S}^{n-1}} g_P} \leq \frac{2}{\alpha^2} \varepsilon$$

leading to $d_H(K, \Omega_\theta) \leq d_H(K, P) + d_H(P, \Omega_\theta) \leq (1 + \frac{2}{\alpha^2}) \varepsilon$. \square

Proof of proposition 2.5. We will use Eq. (1). Let p_θ be a sublinear network.

Case 1 (gauge): assume that $\Omega_\theta := \{x \in \mathbb{R}^d : p_\theta^G(x) \leq 1\}$. For $x \in \Omega_\theta$ and $g \in G$, we have that $p_\theta^G(g.x) = \frac{1}{|G|} \sum_{\tilde{g} \in G} p_\theta(g.\tilde{g}.x) = \frac{1}{|G|} \sum_{\tilde{g} \in G} p_\theta((g\tilde{g}).x) = p_\theta^G(x) \leq 1$ hence $g.\Omega_\theta \subset \Omega_\theta$. We can then deduce the reverse inclusion by $x \in \Omega_\theta \implies g^{-1}.x \in \Omega_\theta \implies x \in g.\Omega_\theta$.

Case 2 (support): assume that $\Omega_\theta := \{x \in \mathbb{R}^d : x \cdot y \leq p_\theta^G(y) \text{ for all } y \in \mathbb{R}^d\}$. For $x \in \Omega_\theta$ and $g \in G$, we have for all $y \in \mathbb{R}^d$:

$$(g.x) \cdot y = x \cdot (g^{-1}.y) \leq p_\theta^G(g^{-1}.y) = p_\theta^G(y)$$

hence $g.\Omega_\theta \subset \Omega_\theta$. The reverse inclusion follows. \square

C Computation of shape quantities

C.1 Geometric–differential quantities

Expression of the normal vector As it has been stated, the normal vector is defined by

$$n_\theta(y) = \frac{(D\phi_\theta)^{-T}(x)n_B(x)}{\|(D\phi_\theta)^{-T}(x)n_B(x)\|}.$$

for $y = \phi_\theta(x)$, $x \in \partial B$. Indeed, if φ is a level set function associated to a smooth set Ω (i.e. $\Omega = \{\varphi \leq 0\}$), then for $y \in \partial\Omega$, the normal vector can be computed as

$$n(y) = \frac{\nabla\varphi(y)}{\|\nabla\varphi(y)\|}.$$

In the case of Ω_θ , the function $\varphi(y) = \|\phi_\theta^{-1}(y)\|^2 - 1$ is an admissible level set function since $\varphi(y) \leq 0 \iff y \in \Omega_\theta$. Computing the gradient leads to $\nabla\varphi(y) = D(\phi_\theta^{-1})^T(y).2\phi_\theta^{-1}(y) = 2(D\phi_\theta)^{-T}(x)x$, from which we deduce the formula by normalization. Notice that we never need the expression of ϕ_θ^{-1} to compute $n_\theta(y)$ when $y = \phi_\theta(x)$.

Numerical computation of the Weingarten map The Weingarten map is defined as

$$\begin{aligned} S_y : T_y\partial\Omega_\theta &\longrightarrow T_y\partial\Omega_\theta \\ v &\longmapsto D_\Gamma n(y).v \end{aligned}$$

where $D_\Gamma n(y)$ is the tangential derivative of n , i.e. the restriction of $Dn(y) \in \mathbb{R}^{d \times d}$ to the tangent space $T_y\partial\Omega_\theta$. In order to compute it numerically, one introduces the Housholder matrix $H_y = I - vv^T$ where

$$v = \frac{n(y) - e_d}{\|n(y) - e_d\|},$$

e_1, \dots, e_d being the canonical basis of \mathbb{R}^d . Hence, $H_y n = e_d$ and in particular, the first $d - 1$ lines of H_y are orthogonal to $n(y)$ and hence forms an orthonormal basis of $T_y\partial\Omega_\theta$. One can then compute $D_{\partial\Omega_\theta} n(y)$ in this basis as

$$D_{\partial\Omega_\theta} n(y) = \tilde{H}_y Dn(y) \tilde{H}_y^T \in \mathbb{R}^{(d-1) \times (d-1)}$$

where $\tilde{H} = (H_{ij})_{\substack{1 \leq i \leq d-1 \\ 1 \leq j \leq d}}$.

C.2 Method of fundamental solutions

An important special case of Eq. (5) is the case where f is identically equal to 1, i.e.

$$\begin{cases} -\Delta u &= 1 & \text{in } \Omega_\theta, \\ u &= 0 & \text{on } \partial\Omega_\theta. \end{cases} \quad (7)$$

In this case, the solution $u \in H_0^1(\Omega_\theta)$ is called the *torsion function*, which is an important function in mechanics that has been extensively studied in mathematics. One important derived quantity is the *torsional rigidity* defined as

$$T(\Omega_\theta) = \int_{\Omega_\theta} u \quad (8)$$

which describes the rigidity of a rod of cross section Ω_θ .

It is well known that Eq. (7) can be solved in an extremely precise and efficient way using the *method of fundamental solutions* [37, 5, 38]. Indeed, by putting $\phi(x) = u(x) + \frac{x_1^2}{2}$, Eq. (7) can be equivalently reformulated as the following Laplace equation:

$$\begin{cases} -\Delta\phi = 0 & \text{in } \Omega_\theta, \\ \phi = \frac{x_1^2}{2} & \text{on } \partial\Omega_\theta. \end{cases} \quad (9)$$

One may then seek an approximate solution $\tilde{\phi}$ expressed as a linear combination of fundamental solutions, namely,

$$\tilde{\phi}(x) := \sum_{i=1}^n c_i \psi(x - y_i),$$

where ψ is the fundamental solution to $-\Delta\psi = \delta_0$ in $\mathbb{R}^d - \{0\}$ and $y_1, \dots, y_n \in \Omega_\theta^c$ [27]. Since ϕ is harmonic in Ω , we only have to fit the boundary condition, for instance, in an L^2 sense, which amounts at solving

$$\min_{c_1, \dots, c_n \in \mathbb{R}} \int_{\partial\Omega} \left| \tilde{\phi}(x) - \frac{x_1^2}{2} \right|^2 d\sigma.$$

Since this integral cannot be analytically computed for a general Ω , it is discretized and the resulting least squares problem is solved using `torch.linalg.lstsq`.

There exists several valid choices for the placement of the sources y_1, \dots, y_n . In our case, we decided to do it the following way: draw samples $x_1, \dots, x_n \in \partial B$, and set $y_i := \phi_\theta(x_i) + \varepsilon n_\theta(x_i)$ for $\varepsilon > 0$. This way, we have the guarantee that y_i lies outside and at distance ε of Ω_θ . An alternative and more flexible approach in the case where Ω_θ is parametrized by a gauge function Eq. (3) is to take $y_i = \phi_\theta((1 + \varepsilon)x_i)$. This has the advantage that scaling Ω_θ leads to the same scaling of the distance from y_i to Ω_θ .

It is well known that this method is very sensitive to the source placement, and that the conditioning worsens when the number of sources increase. However, this can be mitigated by an *a posteriori* error estimation using the maximum principle: knowing that $\|\phi - \tilde{\phi}\|_\infty := \sup_{\Omega_\theta} |\phi - \tilde{\phi}| = \sup_{\partial\Omega_\theta} |\phi - \tilde{\phi}| = \sup_{x \in \partial\Omega_\theta} \left| \frac{x_1^2}{2} - \tilde{\phi} \right|$, we can estimate the last quantity by sampling a large amount of points on $\partial\Omega_\theta$. If the error is greater than a certain tolerance (taken in our experiments of the order $10^{-4} - 10^{-5}$), we can modify the source placement parameter ε and increase the number of sources until the tolerance is reached.

Remark C.1. *While we decided to treat the case of the Laplace equation for simplicity, this approach can easily be extended to other, more practical settings where we have access to the fundamental solutions of the PDE, like in linearized elasticity [39] for the optimal design of structures or in the Stokes problem [40].*

D Comparison with PINNs

As it has already been stressed, PINNs are not particularly well suited in general for the computation of PDE-constrained shape optimization. However, there is some very specific problems for which they can easily be applied, namely when the objective function is the *Dirichlet energy* of the shape. This is the type of energy that has been considered in [14]. In this section, we will compare the use of PINNs with the other methods previously introduced on a similar problem for which we know the analytical solution.

Consider the following problem:

$$\max_{\substack{\Omega \in \mathcal{K} \\ \text{Vol}(\Omega)=1}} T(\Omega) \quad (10)$$

where T is the torsional rigidity defined in Eq. (8). A foundational result in shape optimization, called the Saint–Venant inequality, states that the solution of this problem is the ball [41].

The Dirichlet energy associated with Eq. (7) is defined as

$$E(\Omega, v) := \frac{1}{2} \int_{\Omega} |\nabla v|^2 - \int_{\Omega} v \quad (11)$$

for $v \in H_0^1(\Omega)$. A fundamental property of the Dirichlet energy is that the minimizer u_{Ω} of $E(\Omega, \cdot)$ is the solution of Eq. (7). Using the fact that $\int_{\Omega} |\nabla u_{\Omega}|^2 = \int_{\Omega} u_{\Omega} = T(\Omega)$, this implies that $E(\Omega, u_{\Omega}) = -\frac{T(\Omega)}{2}$. Hence:

$$\min_{\substack{\Omega \in \mathcal{K}, v \in H_0^1(\Omega) \\ \text{Vol}(\Omega)=1}} E(\Omega, v) = \min_{\substack{\Omega \in \mathcal{K} \\ \text{Vol}(\Omega)=1}} \min_{v \in H_0^1(\Omega)} E(\Omega, v) = \min_{\substack{\Omega \in \mathcal{K} \\ \text{Vol}(\Omega)=1}} E(\Omega, u_{\Omega}) = -\frac{1}{2} \max_{\substack{\Omega \in \mathcal{K} \\ \text{Vol}(\Omega)=1}} T(\Omega),$$

which means that minimizing E in both Ω and v is actually equivalent to Eq. (10). Using the following proposition, we can further reformulate the problem:

Proposition D.1. *Any minimizer (Ω, v) of*

$$\min_{\substack{\Omega \in \mathcal{K}, v \in H_0^1(\Omega) \\ \text{Vol}(\Omega)=1}} E(\Omega, v) \quad (12)$$

is a minimizer of

$$\min_{\Omega \in \mathcal{K}, v \in H_0^1(\Omega)} \frac{E(\Omega, v)}{\text{Vol}(\Omega)^{\frac{d+2}{d}}}. \quad (13)$$

Reciprocally, if (Ω, v) is a minimizer of Eq. (13) then $(\alpha_{\Omega}\Omega, \alpha_{\Omega}^2 v(\cdot/\alpha_{\Omega}))$ where $\alpha_{\Omega} = \text{Vol}(\Omega)^{-1/d}$ is a minimizer of Eq. (12).

Proof. Using the change of variable formula, we can show that for $\alpha > 0$,

$$E(\alpha\Omega, \alpha^2 v(\cdot/\alpha)) = \alpha^{d+2} E(\Omega, v).$$

The proposition follows. \square

Therefore, we can actually drop the volume constraint and instead solve Eq. (13). For a parametrized set Ω_{θ} and $v \in H_0^1(\Omega_{\theta})$, we have

$$E(\Omega_{\theta}, v) = \frac{1}{2} \int_B A_{\theta} \nabla(v \circ \phi_{\theta}^{-1}) \cdot \nabla(v \circ \phi_{\theta}^{-1}) - \int_B (\text{Jac}\phi_{\theta})(v \circ \phi_{\theta}^{-1});$$

moreover, minimizing this last expression with respect to $v \in H_0^1(\Omega_{\theta})$ is equivalent to minimizing

$$F(\Omega_{\theta}, v) = \frac{1}{2} \int_B A_{\theta} \nabla v \cdot \nabla v - \int_B (\text{Jac}\phi_{\theta})v.$$

for $v \in H_0^1(B)$. Finally, by taking v to be a neural network v_{η} where η are its parameters, we can approximate Eq. (10) by equivalently minimizing the loss

$$L(\theta, \eta) := \frac{F(\Omega_{\theta}, v_{\eta})}{\text{Vol}(\Omega)^{\frac{d+2}{d}}}.$$

Remark D.1. *In order to exactly impose the Dirichlet boundary condition on ∂B , we chose v_{η} of the form $v_{\eta}(x) = \text{dist}_B(x) \text{MLP}_{\eta}(x)$ where dist_B is the signed distance function of B .*

This approach follows the line of the so-called *Deep Ritz Method* [42]. In opposition to what was previously described in this paper and to classical shape optimization algorithms, one does not need to fully solve the state equation before updating the shape; the state and the shape are jointly optimized, and one can expect v_{θ} to be close to the solution of the state equation only at convergence. Since we do not have to solve a PDE at each iteration, one could expect a certain speedup of this method compared to classical ones; it is however not the case, as is shown in the next experiment.

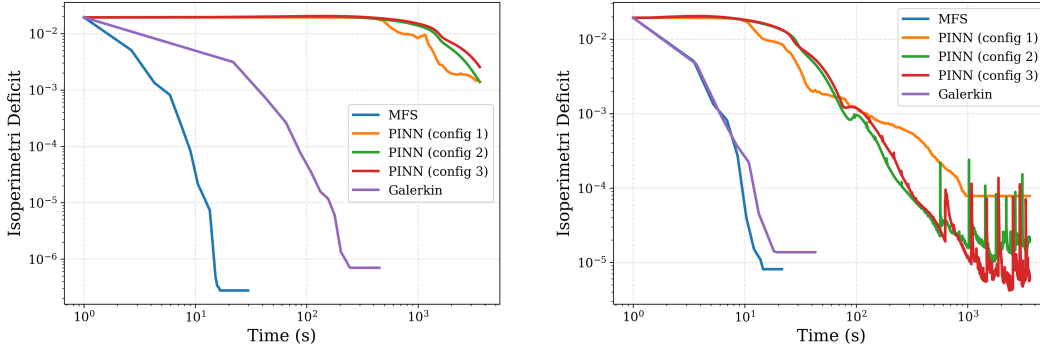


Figure 6: Runtime vs accuracy comparison between classical solvers and PINN-based approaches (CPU/GPU). Classical methods achieve higher accuracy at significantly lower computational cost.

Evaluation of the method: We compare the speed and accuracy of the previously described method with the maximization of $\frac{T(\Omega_\theta)}{\text{Vol}(\Omega_\theta)^{\frac{d+2}{d}}}$ where $T(\Omega_\theta)$ is computed using either the method of fundamental solutions or the mesh free Galerkin method. While the former is expected to be extremely fast and accurate, it doesn't generalize well to other problems with non-constant source term. On the contrary, the latter is expected to be slower due to the fact that it is not taylor to this particular problem; the tradeoff being that it is able to treat a large variety of problems.

Since we know that the optimal shape is the ball, we can measure the discrepancy between the shape Ω_θ and B using the *isoperimetric deficit* [43], defined as

$$D(\Omega_\theta) = c_d \frac{\text{Per}(\Omega_\theta)}{\text{Vol}(\Omega_\theta)^{\frac{d-1}{d}}} - 1$$

with $c_d = (d\text{Vol}(B))^{1/d} - 1$. The smallest the isoperimetric deficit, the closest Ω_θ is from the ball.

In order to give the best advantage to the PINN approach, we first perform a hyperparameter search for the PINN-based method. The tested parameters are given in Table 2, along with the two best configurations, that we picked in our final experiment. The number of points used for integral evaluation is the same across all experiments ($n = 20000$). The evaluation of the perimeter and volume for the computation of the isoperimetric deficit is made using $n = 100000$ points. On the 72 possible choices of parameters, only 3 reached the precision of 10^{-5} eventually; we decided to keep the three of them to compare with the classical methods. These configurations are described in Table 2.

Table 2: Hyperparameter search space (left) and best configurations that are kept for the final experiment.

Hyperparameter	Values	Config 1	Config 2	Config 3
Neurons per layer	{32, 64}	32	32	32
Depth	{2, 3, 4}	3	3	2
Activation Function	{ sin, tanh }	tanh	tanh	tanh
Optimizer	{ Adam, L-BFGS }	L-BFGS	Adam	Adam
Learning rate	{ 10^{-1} , 10^{-2} , 10^{-3} }	10^{-2}	10^{-2}	10^{-2}

In Fig. 6, we show the comparison between the two classical methods and the three PINN-based ones, both on CPU (AMD Ryzen Pro 7) and on GPU (Nvidia L40). We see that the classical methods consistently outperforms the PINN-based one; interestingly enough, both classical methods ran on CPU are still faster and more accurate than the PINN-based methods ran on GPU. This experiment show that, even in the most favorable setting, the PINN approach is outperformed by the classical methods by several orders of magnitude.

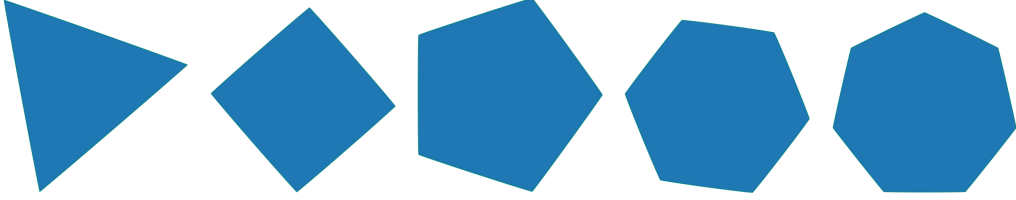


Figure 7: Minimizers of the Mahler volume under n -fold symmetry constraints. The method recovers polygonal structures, highlighting its ability to represent non-smooth convex shapes.

E Minimization of the Mahler volume

Gauge and support functions are related to each other through the notion of *polar body*. The polar body of a convex set $K \in \mathcal{K}$ is defined as $K^\circ := \{x \in \mathbb{R}^d : x \cdot y \leq 1 \text{ for all } y \in K\}$. Then, the gauge function of K is the support function of K° (see [20, Lemma 1.7.13]), i.e. $g_K = h_{K^\circ}$.

In this section, we are interested in the minimization of the *Mahler volume* which is the product of the volumes of a convex Ω and its polar body Ω° , i.e. $\text{Vol}_M(\Omega) := \text{Vol}(\Omega)\text{Vol}(\Omega^\circ)$. Our framework allows us to easily compute both volumes using simultaneously the support and the gauge parametrization.

In \mathbb{R}^d , it is known that the convex set with n -fold rotational symmetry that minimizes the Mahler volume is the regular polygon, and the optimal value is $n^2 \sin(\pi/n)^2$ [44]. Using our parametrization of symmetric convex sets, we get the results presented in Fig. 7. As you can see, our parametrization is flexible enough to recover polygons.

F Statistical Analysis

We complement the experiments of Section 4.1 with a statistical evaluation of robustness to noise. For each configuration (shape and noise level), we perform the following procedure. We randomly initialize the sublinear network p_θ , sample $n = 1000$ points $y_{i=1}^n$, and optimize the loss defined in Section 4.1.

To quantify reconstruction quality, we measure the L^2 discrepancy between the learned function p_θ and the gauge function of the target shape g_{target} . Since $g_{\text{target}} = 1$ on $\partial\Omega_{\text{target}}$, this reduces to

$$\text{Acc}(\theta) = \|g_{\text{target}} - p_\theta\|_{L^2(\partial\Omega_{\text{target}})} = \|p_\theta - 1\|_{L^2(\partial\Omega_{\text{target}})}$$

We approximate this quantity by sampling 10^5 points uniformly on ∂B and mapping them via ϕ_{target} .

Each experiment is repeated 100 times with independent random initializations and samples. We report the median performance together with the interquartile range (25th–75th percentiles). The aggregated results are shown in Fig. 8.

In a second experiment, we analyze the influence of the number of samples on the reconstruction. We fix the noise level to $\sigma = 0.01$ and use different amount of points n ranging from 10 to 10^4 . The results are reported in Fig. 9.

G Integration of the finite element method

Assume that we want to minimize a certain shape function J , depending on a PDE that we would like to solve using the finite element method. While possible, it requires to compute certain derivatives manually.

Defining $j(\theta) := J(\Omega_\theta)$, we want to relate the derivatives $\partial_{\theta_k} j(\theta)$ with the shape derivative $dJ(\Omega_\theta).V$. According to [45, Chapter 5, Section 5.9], under some mild regularity assumptions, shape derivatives can be put in the form

$$dJ(\Omega).V = \int_{\partial\Omega} f(x)V(x) \cdot n_\Omega(x) \quad (14)$$

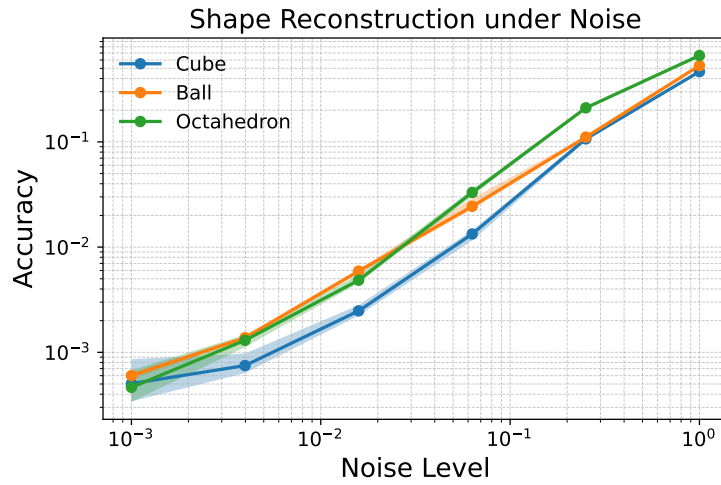


Figure 8: Robustness to noise and network initialization across 100 runs. Median reconstruction error with interquartile range. The method exhibits low variance and stable performance across noise levels.

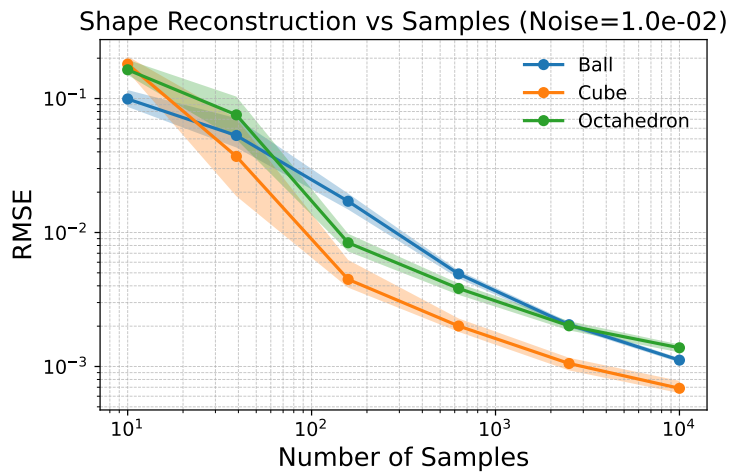


Figure 9: Robustness to amounts of samples and network initialization across 100 runs. Median reconstruction error with interquartile ranges. As expected, the variance is higher when using fewer samples.

where $f : \partial\Omega \rightarrow \mathbb{R}$ depends on Ω . This formula is particularly well suited when one needs to compute f via a mesh-based. Now, let $\theta = (\theta_1, \dots, \theta_n) \in \mathbb{R}^d$ and define $\bar{\theta}(t) := (\theta_1, \dots, \theta_k + t, \dots, \theta_n)$. Following [45, Chapter 5, Section 5.2], define

$$\Phi(t)(x) = \phi_{\bar{\theta}(t)} \circ \phi_{\theta}^{-1}(x)$$

for $t \in \mathbb{R}$ and $x \in \Omega_{\theta}$. We have $\Phi(t)(\Omega_{\theta}) = \phi_{\bar{\theta}(t)} \circ \phi_{\theta}^{-1}(\Omega_{\theta}) = \phi_{\bar{\theta}(t)} \circ \phi_{\theta}^{-1} \circ \phi_{\theta}(B) = \Omega_{\bar{\theta}(t)}$. Hence, by letting $V := \Phi'(0)$, we have by definition of the shape derivative that

$$dJ(\Omega_{\theta}) \cdot V = \lim_{t \rightarrow 0} \frac{J(\Omega_{\bar{\theta}(t)}) - J(\Omega_{\theta})}{t} = \lim_{t \rightarrow 0} \frac{j(\bar{\theta}(t)) - j(\theta)}{t} = \partial_{\theta_k} j(\theta).$$

On the other hand,

$$V(x) = \Phi'(0)(x) = \left. \frac{d\phi_{\bar{\theta}(t)} \circ \phi_{\theta}^{-1}(x)}{dt} \right|_{t=0} = \partial_{\theta_k} \phi_{\theta}(\phi_{\theta}^{-1}(x)),$$

meaning that formally, we have

$$\partial_{\theta_k} j(\theta) = \int_{\partial\Omega_{\theta}} f(x) \partial_{\theta_k} \phi_{\theta}(\phi_{\theta}^{-1}(x)) \cdot n_{\Omega_{\theta}}(x) dx. \quad (15)$$

If ϕ_{θ}^{-1} is easily computable (which is the case, for instance, for Eq. (3) of inverse $\phi_{\theta}^{-1}(y) = \frac{p_{\theta}(y)}{\|y\|} y$) and one can precisely evaluate the boundary integral (for instance, if we have a mesh) then this integral can be easily computed. Otherwise, one can formulate it on the reference domain:

$$\begin{aligned} \partial_{\theta_k} j(\theta) &= \int_{\partial B} f(\phi_{\theta}(x)) \partial_{\theta_k} \phi_{\theta}(\phi_{\theta}^{-1}(\phi_{\theta}(x))) \cdot n_{\Omega_{\theta}}(\phi_{\theta}(x)) \text{Jac}_{\partial B}(\phi_{\theta}(x)) dx \\ &= \int_{\partial B} (f \circ \phi_{\theta}) \partial_{\theta_k} \phi_{\theta} \cdot \frac{(D\phi_{\theta})^{-T} n_B}{|(D\phi_{\theta})^{-T} n_B|} \text{Jac}_{\partial B}(\phi_{\theta}) \\ &= \int_{\partial B} (f \circ \phi_{\theta}) \partial_{\theta_k} \phi_{\theta} \cdot (D\phi_{\theta})^{-T} n_B \text{Jac}(\phi_{\theta}) \end{aligned}$$

An example of optimal sets using this method can be found in Fig. 10, where we minimize the first 6 Dirichlet eigenvalues under volume and convexity constraint. Specifically, we solve:

$$\min_{\text{Vol}(\Omega)=1} \lambda_k(\Omega) \quad (16)$$

where $\Omega \in \mathcal{K}$ and $\lambda_k(\Omega)$ is the k -th Dirichlet eigenvalue, i.e. it solves

$$\begin{cases} -\Delta u = \lambda_k(\Omega) u & \text{in } \Omega \\ u = 0 & \text{on } \partial\Omega \end{cases} \quad (17)$$

for some $u \in H_0^1(\Omega)$. This particular problem has already been considered in [5].

In order to compute the derivatives Eq. (15) of λ_k , we created a mesh of the domain Ω_{θ} using `gmsh` [46], by giving it a sequence of points $y_i = \phi_{\theta}(x_i)$ where $x_i = (\cos(2i\pi/n), \sin(2i\pi/n))^T$, $1 \leq i < n$. An eigenpair $\lambda(\Omega_{\theta}), u(\Omega_{\theta})$ is computed via finite elements using `scikit-fem` [47]. Using the Hadamard expression for the shape derivative $d\lambda(\Omega) \cdot V = \int_{\partial\Omega} |\nabla u|^2 (V \cdot n)$, we deduce that

$$\partial_{\theta_k} j(\theta) = \int_{\partial\Omega_{\theta}} |\nabla u(x)|^2 \partial_{\theta_k} \phi_{\theta}(\phi_{\theta}^{-1}(x)) \cdot n_{\Omega_{\theta}}(x) dx.$$

The differential quantity $\nabla u(x)$ is computed on the finite element space, while $\partial_{\theta_k} \phi_{\theta}$ is computed using AD. The integral is computed on the boundary mesh by `scikit-fem`. All of this process is wrapped in `torch.autograd.Function` in order to seamlessly integrate it into PyTorch's AD.

You can see the six optimal shapes found by the algorithm in Fig. 10 along with the corresponding eigenvalue and the relative error $E_{\text{rel}} := \frac{\lambda_k - \lambda_k^*}{\lambda_k^*}$ where λ_k^* is either the optimal value obtained numerically in [5] or the analytical one for $k = 1$ and $k = 3$ where the optimal shape is known to be the ball. We see that the shapes are in good agreement with the previous results, and that the relative error is of order -3 to -4 .

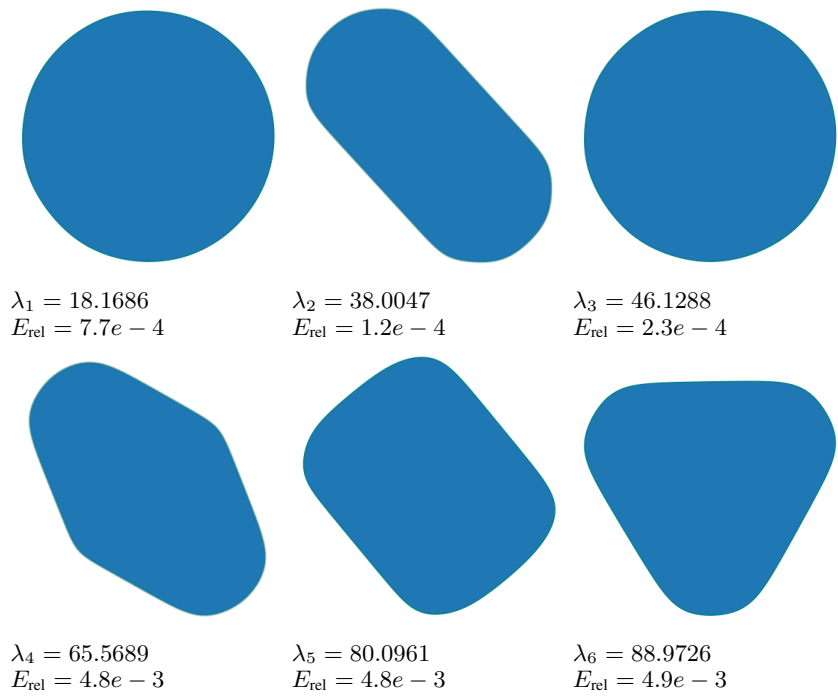


Figure 10: Optimal shapes for the first six Dirichlet eigenvalues